JACS
JOURNAL OF THE AMERICAN CHEMICAL SOCIETY

Article

Isolation of Cu Atoms in Pd Lattice: Forming Highly Selective Sites for Photocatalytic Conversion of CO2 to CH4

Ran Long, Yu Li, Yan Liu, Shuangming Chen, Xusheng Zheng, Chao Gao, Chaohua He, Nanshan Chen, Zeming Qi, Li Song, Jun Jiang, Junfa Zhu, and Yujie Xiong

J. Am. Chem. Soc., **Just Accepted Manuscript** • DOI: 10.1021/jacs.7b00452 • Publication Date (Web): 09 Mar 2017

Isolation of Cu Atoms in Pd Lattice: Forming Highly Selective Sites for Photocatalytic Conversion of CO_2 to CH_4

Ran Long,[⊥] Yu Li,[⊥] Yan Liu,[⊥] Shuangming Chen, Xusheng Zheng, Chao Gao, Chaohua He, Nanshan Chen, Zeming Qi, Li Song, Jun Jiang, Junfa Zhu, and Yujie Xiong*

Hefei National Laboratory for Physical Sciences at the Microscale, *i*ChEM (Collaborative Innovation Center of Chemistry for Energy Materials), School of Chemistry and Materials Science, Hefei Science Center (CAS), and National Synchrotron Radiation Laboratory, University of Science and Technology of China, Hefei, Anhui 230026, P. R. China.

KEYWORDS. Photocatalysis; carbon dioxide; methane; active sites; copper.

Supporting Information Placeholder

ABSTRACT: Photocatalytic conversion of CO_2 to CH_4 – a carbon-neutral fuel represents an appealing approach to remedy the current energy and environmental crisis; however, it suffers from the large production of CO and H_2 by side reactions. The design of catalytic sites for CO_2 adsorption and activation holds the key to address this grand challenge. In this article, we develop highly selective sites for photocatalytic conversion of CO_2 to CH_4 by isolating Cu atoms in Pd lattice. According to our synchrotron-radiation characterizations and theoretical simulations, the isolation of Cu atoms in Pd lattice can play dual roles in the enhancement of CO_2-to-CH_4 conversion: (1) providing the paired Cu-Pd sites for the enhanced CO_2 adsorption and the suppressed H_2 evolution; and (2) elevating the *d*-band center of Cu sites for the improved CO_2 activation. As a result, the Pd_7Cu_1-TiO_2 photocatalyst achieves the high selectivity of 96 % for CH_4 production with a rate of 19.6 μmol g_{cat}^{-1} h^{-1}. This work provides fresh insights into the catalytic site design for selective photocatalytic CO_2 conversion, and highlights the importance of catalyst lattice engineering at atomic precision to catalytic performance.

INTRODUCTION

A significant increase in atmospheric carbon dioxide (CO_2) levels during the past decades has been widely recognized as a global environment problem.[1] For this reason, a large number of investigations have been performed for the reduction of CO_2.[1-6] In particular, the photocatalytic conversion of carbon dioxide with water into methane ($CO_2 + 8H^+ + 8e^- \rightarrow CH_4 + 2H_2O$) is an appealing approach, which allows the transformation of CO_2 into a carbon-neutral fuel by harvesting solar energy.[7-13] Despite the promising future, this approach has faced a grand challenge in terms of reaction activity and selectivity. The activity and selectivity have yet to be significantly improved for two reasons: (1) CO_2 molecules possess very low reactivity in chemical transformations, limiting the catalytic activity; and (2) multiple side reactions such as the reduction of CO_2 to CO and the H_2 evolution from H_2O reduction simultaneously take place, lowering the reaction selectivity.

Like many other catalytic systems, the efficiency of CO_2-to-CH_4 conversion relies on the catalytic sites on photocatalyst surface.[7] Cu has been previously identified as a metal which can provide active sites for CO_2 conversion.[1,4,14,15] In addition to the activity and selectivity issues, the metallic Cu materials at the nanoscale heavily suffer from oxidation. Although Cu nanoparticles can be stabilized by capping agents such as oleylamine,[16] the Cu atoms would be rapidly oxidized once the capping agents are removed prior to catalysis. Given this situation, we decide to adopt an alloying strategy for overcoming this limitation. Alloying Cu with Pd can significantly enhance the resistance of nanoparticles to oxidation.[17, 18] Another important reason for choosing Pd in the alloys is the limited activity of Pd in H_2 evolution.[19-21] The strong binding of H atoms to Pd would suppress the side reaction of H_2 production during the photocatalytic conversion of CO_2 with H_2O.

More importantly, the alloying strategy would also provide an opportunity for improving the activity and selectivity of CO_2 conversion from the angle of lattice engineering. The surface and electronic structures related to catalytic sites are two versatile knobs for tuning the catalytic activity and selectivity, both of which can be tailored by lattice engineering. The metal alloys can supply various local atomic arrangements on surface, which offers the capability of maneuvering adsorption configuration.[22-24] Meanwhile, the compositions in alloys hold the key to tuning the *d*-band centers of active sites.[5,25-27] Taken together, controllable lattice engineering in Cu-based alloys should be a promising approach to the giant enhancement on CO_2 conversion activity and selectivity.

Herein, we report that the Pd_xCu_1 alloys with Cu atoms isolated in Pd lattice can provide highly active sites for the enhanced CO_2 adsorption and activation. The active sites, the paired Cu-Pd atoms with tunable *d*-band centers, enable the dramatically enhanced activity and selectivity in the photocatalytic reaction of CO_2 with H_2O. As a proof of concept, the Pd_7Cu_1-TiO_2 photocatalyst achieves the high selectivity of 96 % for CH_4 production rate with a rate of 19.6 μmol g_{cat}^{-1} h^{-1}. This work offers a lattice engineering approach to boosting the selectivity in photocatalytic CO_2 conversion.

EXPERIMENTAL SECTION

Synthesis of Pd_xCu_1-TiO_2 hybrid structures. In a typical synthesis, 8 mL of an aqueous solution containing 100 mg of TiO_2 nanosheets was sonicated for 20 min in a 50-mL glass vial. Then 105 mg of polyvinylpyrrolidone (PVP, M.W. = 55,000), 120 mg of ascorbic acid (AA), and 300 mg of KBr were added into the glass vial under magnetic stirring in an oil bath preset to 80 °C for 10 min. Subsequently, certain amounts of K_2PdCl_4 (0.100 mmol, 0.150 mmol, 0.167 mmol, 0.175 mmol, 0.180 mmol, and 0.183 mmol in 3 mL water) and $CuCl_2{\cdot}2H_2O$ (0.100 mmol, 0.050 mmol, 0.033 mmol, 0.025 mmol, 0.020 mmol, and 0.0167 mmol in 1 mL water) solutions were injected into the reaction solution. The reaction mixture was heated at 80 °C in air for 3 h. The samples were washed with water several times to remove most of the AA and PVP by centrifugation. The obtained samples were denoted as Pd_1Cu_1-, Pd_3Cu_1-, Pd_5Cu_1-, Pd_7Cu_1-, and $Pd_{11}Cu_1$-TiO_2, respectively, according to the amounts of added K_2PdCl_4 and $CuCl_2$ solutions.

XAFS characterization. Cu *K*-edge and Pd *K*-edge X-ray absorption fine structure (XAFS) measurements were performed at the beamline 14W1 in Shanghai Synchrotron Radiation Facility (SSRF), China. The X-ray was monochromatized by a double-crystal Si(311) monochromator. The storage ring of SSRF was operated at 3.5 GeV with the current of 300 mA. The acquired extended XAFS (EXAFS) data were processed according to the standard procedures using the WinXAS3.1 program.[28] Theoretical amplitudes and phase-shift functions were calculated with the FEFF8.2 code using the crystal structural parameters of the Cu foil, CuO and Pd foil.[29]

XPS characterization. X-ray photoelectron spectroscopy (XPS) experiments were performed at the Photoemission Endstation at the BL10B beamline in the National Synchrotron Radiation Laboratory (NSRL) in Hefei, China. This beamline was connected to a bending magnet and equipped with three gratings that cover photon energies from 100 to 1000 eV with a typical photon flux of 1×10^{10} photons s^{-1} and a resolution ($E/\Delta E$) better than 1,000 at 244 eV. The endstation comprised four chambers including analysis chamber, preparation chamber, high-pressure reactor and load-lock chamber. The base pressures for the four chambers were 2×10^{-10}, 2×10^{-10}, 5×10^{-9}, and 5×10^{-9} mbar, respectively. The analysis chamber was connected to the beamline and equipped with a VG Scienta R3000 electron energy analyzer, a twin-anode X-ray source(Mg *Ka* and Al *Ka*), a UV light source, a rear-view optics for low-energy electron diffraction (LEED), and a high-precision manipulator with four-degree-of-freedom (X, Y, Z, R for changing polar angle (θ)). The preparation chamber comprised an Ar^+ sputter ion gun, a quartz crystal microbalance (QCM), a quadrupole mass spectrometer (Pfeiffer QMS220), a high precision manipulator with four-degree-of-freedom (X, Y, Z and R), and several evaporators. The high-pressure reactor performed the *in-situ* high-pressure experiments under different atmosphere conditions with a maximum range of 2 MPa and a highest temperature of 650 °C.

***In-situ* DRIFTS characterization.** *In-situ* diffuse reflectance infrared Fourier-transform spectroscopy (DRIFTS) measurements were performed using a Bruker IFS 66v Fourier-transform spectrometer equipped with a Harrick diffuse reflectance accessory at the Infrared Spectroscopy and Microspectroscopy Endstation (BL01B) in National Synchrotron Radiation Laboratory (NSRL), Hefei. Each spectrum was recorded by averaging 256 scans at a 2 cm^{-1} spectral resolution. The samples were held in a custom-fabricated IR reaction chamber which was specifically designed to examine highly scattering powder samples in the diffuse reflection mode. The chamber was sealed with two ZnSe windows. During the *in-situ* characterization, 0.2 MPa of CO_2 was introduced into the chamber, and the peaks of free molecular CO_2 were set as a reference between the samples.

Photocatalytic CO_2 conversion measurement. The measurement was performed using our previously developed stainless-steel photocatalytic reactor.[30] In the reactor, the quartz tube had a length of 320 mm and an inner diameter of 20 mm. The total volume of the reactor was about 100 mL. A 300-W Xe lamp (SolarEdge700, China) with a 400-nm short-wave-pass cutoff filter (i.e., $\lambda < 400$ nm) was used as the light source and positioned above the photocatalytic reactor. The power density was measured to be 2 $mW{\cdot}cm^{-2}$. The catalysts (5 mg of TiO_2 loaded with 0.01 mmol of metal atoms) were mounted above a small quartz beaker containing 1 mL of water and placed in a quartz tube. The photocatalytic reaction was typically performed for 2 h with 0.2 MPa of CO_2 to calculate the average rates for gas production. The amounts of CH_4, CO and H_2 evolved were determined using gas chromatograph (GC, 7890A, Ar carrier, Agilent). H_2 was detected using a thermal conductivity detector (TCD). The CH_4 was measured by a flame ionization detector (FID). The CO was converted to CH_4 by a methanation reactor and then analyzed by the FID. The isotope-labelled experiments were performed using $^{13}CO_2$ instead of $^{12}CO_2$, and the products were analyzed using gas chromatography-mass spectrometry (GC-MS, 7890A and 5975C, Agilent).

First-principles simulations. Spin-polarized density functional theory (DFT) calculations were performed with the Vienna ab initio simulation package (VASP).[31] Perdew-Burke-Ernzerhof (PBE) exchange-correlation functional and projector augmented-wave (PAW) potential were employed. An energy cutoff of 400 eV was used for the

plane-wave expansion of the electronic wave function. The force and energy convergence criterion were set to be 0.01 eV Å^{-1} and 10^{-5} eV, respectively. A 2 × 2 slab with five atomic layers was employed to model the Pd-Cu (100) surfaces, of which two bottom layers were fixed to their bulk positions during the geometry optimizations. A 7 × 7 × 1 k-points grid was adopted for the first Brillouin zone using gamma center sampling scheme. The periodic boundary condition (PBC) was set with a 25 Å vacuum layer in the c direction to isolate surfaces in adjacent slabs. The adsorption energy E_{ads} is defined as: $E_{ads} = E_{total} - E_{surface} - E_{CO_2}$, where E_{total}, $E_{surface}$, and E_{CO_2} stand for the energy of adsorption configurations, the energy of metallic surfaces, and the energy of molecular CO_2, respectively. In the simulation, we have considered several configurations for the adsorbed CO2 molecule. According to the adsorption energy, the most favorable configurations are presented.

RESULTS AND DISCUSSION

The Pd_xCu_1 alloy nanocrystals with a face-centered cubic (*fcc*) phase are *in-situ* grown on anatase TiO_2 nanosheets through an aqueous solution synthesis similarly to the protocol for Pd-TiO_2 hybrid structures,[32, 33] in which the atomic ratios of Pd to Cu can be controlled by adjusting the concentrations of Pd and Cu precursors. As shown in Figures 1 and S1, the namely Pd_xCu_1-TiO_2 hybrid structures have Pd_xCu_1 alloy nanocrystals supported on TiO_2 nanosheets. The Pd_xCu_1 alloy nanocrystals display a truncated cubic profile with the average edge length of 6 nm, and the TiO_2 nanosheets have edge lengths of 50-70 nm and thickness of 6-10 nm. While their crystal phases are confirmed by X-ray diffraction (XRD, Figure S2), we employ inductively-coupled plasma mass spectrometry (ICP-MS) to determine the molar ratios of Pd to Cu in the samples. As listed in Table S1, the content of Cu in Pd_xCu_1 alloys can be controlled in a certain range up to 50 %, beyond which the formed product becomes unstable. As a result, we obtain a series of samples (namely, Pd_1Cu_1-, Pd_3Cu_1-, Pd_5Cu_1-, Pd_7Cu_1-, Pd_9Cu_1-, and $Pd_{11}Cu_1$-TiO_2) with various atomic ratios of Pd to Cu and comparable total molar contents of Pd and Cu (11-13 %). XPS measurements (Figure S3) indicate that the Pd and Cu elements in the samples are of zero valence; however, too high Cu content makes the Pd_xCu_1 nanocrystals more susceptible to oxidation.

Figures 1a and 1b display the transmission electron microscopy (TEM) images of two typical samples with different Cu contents – Pd_1Cu_1-TiO_2 and Pd_7Cu_1-TiO_2, showing that the Pd_xCu_1 alloy nanocrystals with comparable shapes and sizes are loaded on TiO_2 nanosheets regardless the content of Cu atoms. Atomic-resolution aberration-corrected high-angle annular dark-field scanning TEM (HAADF-STEM, Figures 1c and 1d) images show that the Pd_1Cu_1 and Pd_7Cu_1 have the lattice fringes with a spacing of 1.9 and 2.0 Å, respectively, which can be assigned to the (200) planes of *fcc* Pd-Cu alloys. The incorporation of more Cu atoms into Pd lattice slightly reduces the lattice constant. To resolve the spatial distribution of Pd and Cu elements, we have collected energy-dispersive X-ray spectroscopy (EDS) line scans on the alloy nanocrystals. As revealed by Figures 1e and 1f, Pd and Cu elements are nearly distributed at the same locations, suggesting the formation of alloys.

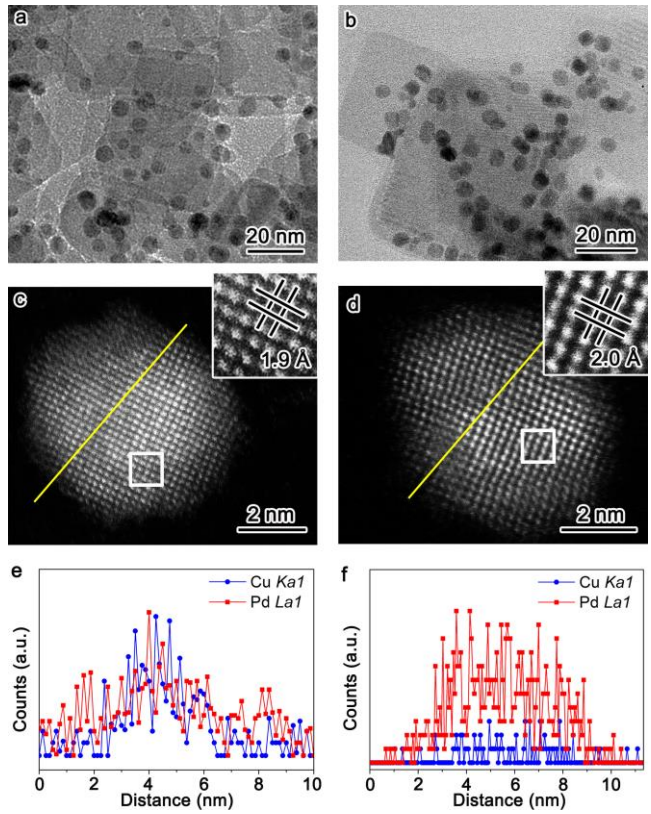

Figure 1. TEM images of (a) Pd_1Cu_1-TiO_2 and (b) Pd_7Cu_1-TiO_2 hybrid structures. HAADF-STEM images of (c) Pd_1Cu_1 and (d) Pd_7Cu_1. The insets of c and d show the atomic-resolution images taken from the regions marked by the boxes. EDS line mapping profiles of (e) Pd_1Cu_1 and (f) Pd_7Cu_1 along the directions marked by the yellow lines in c and d, respectively.

To precisely resolve the local structural information for Pd and Cu atoms, the samples are further characterized by synchrotron radiation-based X-ray absorption fine structure (XAFS) spectroscopy. Figures 2a and 2b show the Cu and Pd *K*-edge X-ray absorption near-edge structure (XANES) spectra of Pd_1Cu_1, Pd_7Cu_1 and $Pd_{11}Cu_1$ in reference to standard Cu and Pd foil. Processed through a Fourier-transform (FT), the Cu and Pd *K*-edge extended XAFS (EXAFS) spectra are obtained. The main peak in the Cu *K*-edge spectra of Pd_xCu_1 samples (Figure 2c) fits the characteristics of Pd-Pd bond instead of Cu-Cu bond, indicate that Cu atoms are mostly coordinated with Pd atoms in the Pd lattice. Moreover, the emerging shoulder peaks in the Cu *K*-edge spectra of Pd_xCu_1 samples indicate that the surface Cu atoms are slightly oxidized particularly for the Pd_1Cu_1 with relatively high Cu content. In comparison, the Pd *K*-edge spectra of Pd_xCu_1 samples (Figure 2d) do not show distinct difference from that of Pd foil, except for the slightly reduced amplitude. This local

structural information indicates that the Pd atoms mainly retain the original Pd lattice.

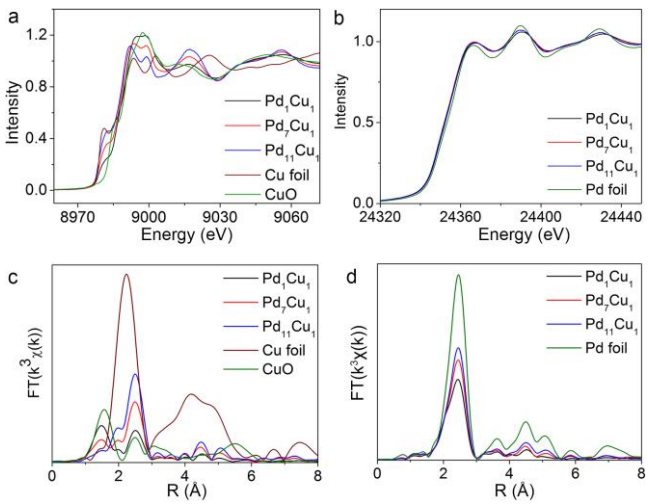

Figure 2. Normalized (a) Cu *K*-edge and (b) Pd *K*-edge XANES spectra of Pd_1Cu_1, Pd_7Cu_1 and $Pd_{11}Cu_1$ in reference to Cu foil and Pd foil. k^3-weighted Fourier-transform (c) Cu *K*-edge and (d) Pd *K*-edge EXAFS spectra.

To look into bonding information, we extract metal-metal bond lengths and metal coordination numbers from EXAFS curve fitting. It is known that the atoms inside an *fcc* lattice are fully coordinated to have the coordination number of 12, while the surface atoms are coordinately unsaturated with a coordination number of 7, 8, and 9 for (110), (100), and (111) facet, respectively. With the crystal sizes are shrunk to the nanoscale, the proportion of surface atoms should be boosted. In our case, the average particle size of Pd_xCu_1 alloy nanocrystals is about 6 nm, which makes the total coordination number substantially less than 12 particularly for Cu atoms. As listed in Table 1, the oxidation of Cu obviously occurs when the Cu concentration is at a relatively high level in Pd_1Cu_1. As the content of Cu is reduced below 12.5 % (Pd_7Cu_1 and $Pd_{11}Cu_1$), the oxidation state of Cu are significantly suppressed. Moreover, the Cu-Cu bonds disappear in these two samples, suggesting that the Cu atoms are nearly isolated in Pd lattice when the Cu/Pd ratio is less than 1/7.

Upon acquiring the fine structures, we are now in a position to investigate the efficacy of atomic isolation in the enhancement of photocatalytic CO_2 reduction. Figure 3a shows the average production rates of CH_4 and CO in photocatalytic CO_2 reduction with H_2O by various TiO_2-based samples. By loading Pd_xCu_1 and Pd nanocrystals on TiO_2, the photocatalytic activities have been obviously enhanced. At the same loading amounts, the photocatalytic production rates show a strong correlation with the chemical compositions of the loaded metal nanocrystals. Given that the addition of metal nanocrystals has not altered light absorption (Figure S4), this performance enhancement should be related to the functions of cocatalysts. In principle, the metal nanocrystals integrated with TiO_2 can play a role as cocatalysts for improving charge separation and supplying reaction sites. Figure S5 shows the photocurrents of all samples which can offer an informative evaluation for the efficiency of electron-hole separation. It demonstrates that the addition of Pd_xCu_1 and Pd nanocrystals significantly enhances the photocurrent of TiO_2, suggesting the role of co-catalysts in separating the electron-hole pairs photogenerated in TiO_2 nanosheets. Nevertheless, various Pd_xCu_1 and Pd co-catalysts show very limited difference in the photocurrent enhancement factors, which are in the range of 1.8 to 2.3 times. It indicates that all the co-catalysts can establish valid Schottky junctions with TiO_2 to improve the electron-hole separation. Thus the volcanic relationship between cocatalyst compositions and photocatalytic activities should be directly related to the active sites.

Table 1. Fitting results of Cu and Pd *K*-edge EXAFS data. The lengths of Cu-O, Cu-Cu, Cu-Pd, Pd-Cu, and Pd-Pd bonds and coordination numbers of Cu and Pd atoms are extracted from the curve-fitting for Cu and Pd *K*-edge EXAFS data (Figure 2), respectively. CN, the coordination numbers of Cu and Pd atoms; R, the lengths of Cu-O, Cu-Cu, Cu-Pd, Pd-Cu, and Pd-Pd bonds;σ^2, the Debye-Waller factor. Error bounds (accuracies) are estimated as CN, ±5 %; R, ±1 %; σ^2, ±1 %.

Sample	EXAFS	Bond	CN	R (Å)	σ^2 (10^{-3} Å^2)
Pd_1Cu_1	Cu *K*	Cu-O	2.0	1.91	4.3
		Cu-Cu	0.4	2.59	9.9
		Cu-Pd	3.3	2.66	11.0
	Pd *K*	Pd-Cu	2.3	2.66	11.0
		Pd-Pd	7.1	2.72	7.3
Pd_7Cu_1	Cu *K*	Cu-O	1.2	1.92	3.9
		Cu-Pd	4.7	2.68	9.1
	Pd *K*	Pd-Cu	1.1	2.68	9.1
		Pd-Pd	7.7	2.73	6.8
$Pd_{11}Cu_1$	Cu *K*	Cu-O	0.4	1.89	4.0
		Cu-Pd	6.3	2.69	8.4
	Pd *K*	Pd-Cu	0.7	2.69	8.4
		Pd-Pd	8.0	2.73	6.4
Cu foil	Cu *K*	Cu-Cu	12	2.54	7.4
Pd foil	Pd *K*	Pd-Pd	12	2.74	5.4

Among the photocatalysts, Pd_7Cu_1-TiO_2 achieves the highest performance with a selectivity of 95.9 % and a rate of 19.6 μmol g_{cat}^{-1} h^{-1} for CH_4 production (Table S2). To verify the origins of CH_4 and CO, we have traced the carbon sources in the reactions using a ^{13}C isotopic label. Figure 3b shows the mass spectra of CO and CH_4 products using $^{13}CO_2$ as substrate under identical photocatalytic reaction

conditions. The peaks at m/Z = 29 and m/Z = 17 can be assigned to ^{13}CO and $^{13}CH_4$, indicating that the carbon source of CO and CH_4 indeed originate from the used CO_2. Notably the H_2 evolution from H_2O reduction has been effectively eliminated (Table S2), demonstrating the niche of Pd matrix in cocatalysts. In sharp contrast, bare TiO_2 exhibits a relatively low selectivity of 57.6 % and a production rate of 0.66 μmol g_{cat}^{-1} h^{-1} for CH_4 production. When the Pd-rich nanocrystals are used as cocatalysts, the enhancement of photocatalytic activities is mainly reflected by the facilitated CO production. For instance, the integration of TiO_2 with Pd_1Cu_1 nanocrystals substantially promotes the CO production rate from 0.94 to 2.10 μmol g_{cat}^{-1} h^{-1}, while the production rate for CH_4 stays at 0.70 μmol g_{cat}^{-1} h^{-1}. As a result, the selectivity for CH_4 production drops to 35.4 % (Table S2).

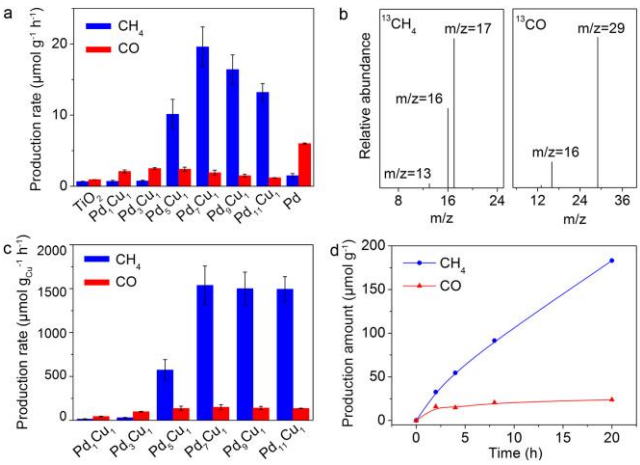

Figure 3. (a) Average production rates of CH_4 and CO in photocatalytic CO_2 reduction with H_2O by bare TiO_2, Pd_1Cu_1-TiO_2, Pd_3Cu_1-TiO_2, Pd_5Cu_1-TiO_2, Pd_7Cu_1-TiO_2, Pd_9Cu_1-TiO_2, $Pd_{11}Cu_1$-TiO_2 and Pd-TiO_2 hybrid structures under UV-light (λ < 400 nm) irradiation with a power density of 2 mW·cm^{-2}. The catalysts are 5 mg of TiO_2 loaded with 0.01 mmol of metal atoms. (b) Mass spectra of $^{13}CH_4$ (m/z = 17) and ^{13}CO (m/z = 29) produced over Pd_7Cu_1-TiO_2 in photocatalytic reduction of $^{13}CO_2$. (c) Average production rates of CH_4 and CO calculated by the amounts of Cu atoms in the Pd_xCu_1-TiO_2 catalysts. (d) Time-dependent production of CH_4 and CO in photocatalytic CO_2 reduction with H_2O by Pd_7Cu_1-TiO_2 up to 20 h.

The CH_4 production can be dramatically promoted by isolating Cu in Pd lattice (Table S2). As the Cu content is diluted to less than 12.5 % (i.e., Pd_7Cu_1), the selectivity for CH_4 production is elevated to the level of about 96 %. According to the XAFS characterization (Table 1), Cu atoms are nearly isolated by the surrounding Pd atoms when reducing the Cu concentrations down below 12.5 %. Thus the isolation of Cu sites in lattice appears to be a powerful approach to improve the selectivity for CH_4 production. However, the production rates are gradually reduced with the further decrease in Cu contents beyond 12.5 %. This decay in production rates should be related to the reduced number of Cu atoms on surface. To support this argument, we normalize the production rates by the amount of Cu atoms. As shown in Figure 3c, the reaction activity per gram of Cu is kept consistent once the Cu atoms are isolated in lattice (i.e., from Pd_7Cu_1 to $Pd_{11}Cu_1$). The isolated Cu atoms can achieve a CH_4 production rate of about 1538 μmol g_{Cu}^{-1} h^{-1}, which turns out to be stable in a continuous 20-hour test (Figure 3d). As indicated by Figure S6, the Pd_7Cu_1-TiO_2 photocatalyst shows excellent durability in seven 4-hour cycles (i.e., 28 hours in total), which can be ascribed to the well-maintained Cu isolation and resistance to oxidation during the photocatalysis (Figure S7 and Table S3).

Since high Cu content makes the Pd_xCu_1 nanocrystals more susceptible to oxidation (Figure S3), a question naturally arises whether the oxidation of Cu sites causes the relatively low activity in photocatalytic CO_2 conversion by Pd_1Cu_1-TiO_2. To examine this possibility, we treat the Pd_1Cu_1-TiO_2 sample with H_2 reduction at 200 °C, which can fully reduce the oxidized Cu atoms to Cu(0) but does not form palladium hydride (Figures S8 and S9). It turns out that the H_2-treated Pd_1Cu_1-TiO_2 still exhibits the same low activity in photocatalytic CO_2 conversion. It indicates that the low activity of Pd_1Cu_1 in CO_2 reduction is not caused by the surface oxidation.

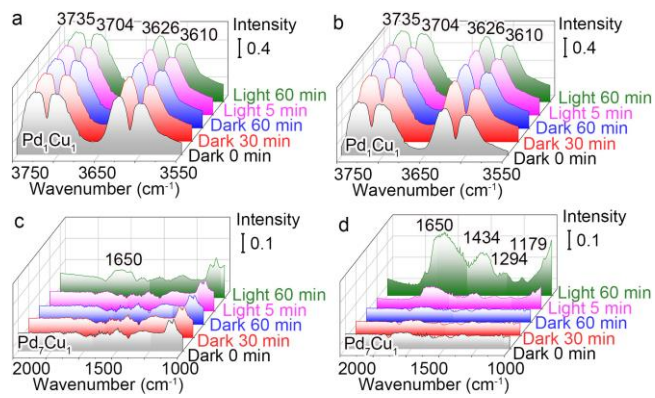

Figure 4. *In-situ* DRIFTS spectra for the adsorption and activation of CO_2 in the presence of H_2O under Xe-lamp irradiation: (a) Pd_1Cu_1-TiO_2 at 3550-3750 cm^{-1}, (b) Pd_7Cu_1-TiO_2 at 3550-3750 cm^{-1}, (c) Pd_1Cu_1-TiO_2 at 1000-2250 cm^{-1}, and (d) Pd_7Cu_1-TiO_2 at 1000-2250 cm^{-1}.

Given this situation, we look into the effects of Pd_xCu_1 atomic arrangements on CO_2 reduction reactivity by employing *in-situ* DRIFTS spectroscopy. The *in-situ* DRIFTS spectroscopy is a powerful technique to gain the local information for reaction species and their intermediates. In our measurement, a reaction chamber for photocatalytic reactions is used. The baselines are deducted from all spectra to exclude environment factors, and the peaks of free molecular CO2 are set as a reference. Based on the identical environment, the intensity difference between the samples can be qualitatively analyzed. The chamber is firstly filled by 0.2-MPa CO_2 for 60 min without incident light. The DRIFTS spectra of both Pd_1Cu_1-TiO_2 (Figure 4a) and Pd_7Cu_1-TiO_2 (Figure 4b) show

broad peaks at 3735 and 3704 cm^{-1} owing to the stretching vibrations of surface OH-Ti^{4+} and OH-Ti^{3+}, respectively,[34] in addition to the vibrations of gas-phase CO_2 (Figures 4c and 4d). The bands located at 3626 and 3610 cm^{-1} can be assigned to the OH stretching vibrations of free HCO_3^- and H_2O, respectively.[35,36]

The chamber is then irradiated by 300-W simulated solar Xe lamp for another 60 min. In the presence of CO_2 and incident light, the vibrations of OH show no distinct changes for both Pd_1Cu_1-TiO_2 and Pd_7Cu_1-TiO_2 hybrid structures (see Figures 4a and 4b). However, the spectra exhibit some significant differences in the range of 1000-1800 cm^{-1} (see Figures 4c and 4d). The exposure of Pd_7Cu_1-TiO_2 to CO_2 and incident light leads to the appearance of several bands, whereas the changes for Pd_1Cu_1-TiO_2 are significantly weaker. On the surface of Pd_7Cu_1-TiO_2, the peaks at 1179 and 1650 cm^{-1} can be assigned to surface bicarbonate HCO_3^- species.[34,35] Note that the broadened peaks may originate from a variety of intermediates formed during the photocatalytic CO_2 conversion. Nevertheless, the peaks at 1294 and 1434 cm^{-1} are in good agreement with the reported values for the generation of CO_2^- and carbonate-like ($CO_3^=$) species.[36,37] The absence of signals in the range of 1800-2000 cm^{-1} indicates that no CO has been detected in gas phase or at catalytic surface.[33,34] Based on the DRIFTS observations, we can conclude that the monatomic Cu sites in Pd matrix lattice significantly enhances the formation of HCO_3^-, CO_2^- and $CO_3^=$ species, which are the most important intermediate states in the reactions of CO_2 conversion as reported in literature.[35-37] In comparison, the signal changes during all adsorption and reaction processes in the spectra for Pd_1Cu_1-TiO_2 are quite weak, which well aligns with its low performance in photocatalytic CO_2 conversion.

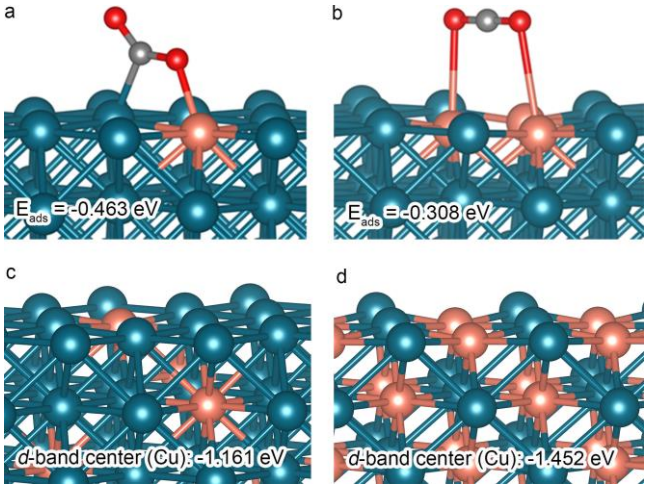

Figure 5. The most favorable configurations and adsorption energies of CO_2 at (a) an isolated Cu atom (i.e., a Cu-Pd pair), and (b) two neighbored Cu atoms (i.e., a Cu-Cu pair). The structural models and Cu *d*-band centers for ordered (c) Pd_7Cu_1 and (d) Pd_1Cu_1 lattices. All the results are obtained by first-principles simulations.

To gain insight into the CO_2 adsorption and activation with Cu atomic isolation, we have employed first-principles simulation[31] to examine the CO_2 adsorption on various Pd_xCu_1 surfaces. In the simulation, we first examine the adsorption states of CO_2 at Pd surfaces with 1 or 3 atoms replaced by Cu, which represent the surfaces with fully isolated Cu sites and neighbored Cu atoms, respectively. With the Cu atom fully isolated by Pd lattice, the CO_2 optimal adsorption configuration takes place at the neighbored Cu-Pd pair with the adsorption energy of -0.463 eV (Figure 5a). In sharp contrast, the adsorption of CO_2 to the neighbored Cu-Cu pair is substantially weaker (-0.308 eV, Figure 5b). It demonstrates that a Cu-Pd atomic pair, which is formed by isolating Cu atoms in Pd lattice, can serve as a highly active site for CO_2 adsorption.

In addition to the surface structures, electronic structures are believed to play an additional role in tuning catalytic activities. We calculate the *d*-band centers of Cu atoms in two ordered lattices – Pd_7Cu_1 (Figure 5c) and Pd_1Cu_1 (Figure 5d), which reveals that the Cu *d*-band center of Pd_7Cu_1 is substantially higher than that of Pd_1Cu_1 (-1.161 *versus* -1.452 eV). The Cu *d*-band centers are tuned through the electronic structure coupling with the surrounding Pd atoms. When a Cu atom is surrounded by more Pd atoms, the electronic structure will be more affected by the Pd atoms to better elevate the *d*-band center of each Cu site. The elevated Cu *d*-band center of Pd_7Cu_1 would increase the catalytic activity of Cu sites. As compared with CO production ($CO_2 + 2H^+ + 2e^- \rightarrow CO + H_2O$), the conversion of CO_2 to CH_4 ($CO_2 + 8H^+ + 8e^- \rightarrow CH_4 + 2H_2O$) requires an 8-electron process to which the enhanced catalytic activity of reaction sites can make an important contribution.

To further demonstrate the importance of Cu isolation to CO_2 activation, we have annealed our Pd_1Cu_1-TiO_2 sample at 300 °C in H_2 atmosphere (see Figure S10 and Table S4). Although this annealing process does not produce the intermetallic B2 phase where Cu sites are completely isolated as reported in literature,[5] a small number of Cu atoms have migrated to become relatively separated. As a result, the annealing treatment has slightly promoted the formation of CH_4 in photocatalysis. This suggests that the isolation of Cu sites should be beneficial to the activation of CO_2 molecules. Our investigation indicates that the isolation of Cu sites can promote the photocatalytic CO_2 reduction regardless of photocatalyst semiconductors. As a demonstration, we have employed $BiVO_4$ as a visible-light photocatalyst for integration with our Pd_xCu_1 cocatalysts. As shown in Figure S11, Pd_7Cu_1-$BiVO_4$ can effectively convert CO_2 into CH_4 with a small amount of CO via photocatalysis under visible irradiation.

CONCLUSION

In conclusion, we have developed highly selective sites for photocatalytic conversion of CO_2 to CH_4 by isolating Cu atoms in Pd lattice. Our synchrotron-radiation characterizations and theoretical simulations reveal that the isolation of Cu atoms in Pd lattice can play multiple

roles in the enhancement of CO_2-to-CH_4 conversion. The incorporation of trace Cu atoms in Pd matrix can form the paired Cu-Pd sites for enhanced CO_2 adsorption and elevate the *d*-band center of Cu sites for improved CO_2 activation. The Pd matrix also makes a contribution to the suppression of a frequently observed side reaction – H_2 evolution. Remarkably, the Pd_7Cu_1 alloy cocatalysts integrated with TiO_2 photocatalysts have achieved the high selectivity of 96 % for CH_4 production with a rate of 19.6 μmol g_{cat}^{-1} h^{-1}. This work represents a step towards the high-selectivity conversion of CO_2 to carbon-neutral fuels. The concept demonstrated here calls for future efforts on lattice engineering at atomic precision for catalysts design towards solar-driven CO_2 conversion.

ASSOCIATED CONTENT

Supporting Information. Detailed experimental section, characterization methods, and additional material characterizations. This material is available free of charge via the Internet at http://pubs.acs.org.

AUTHOR INFORMATION

Corresponding Author

*yjxiong@ustc.edu.cn

Author Contributions

⊥These authors contributed equally.

Notes

The authors declare no competing financial interest.

ACKNOWLEDGMENT

This work was financially supported in part by 973 Program (No. 2014CB848900), NSFC (No. 21471141, U1532135, 21601173), CAS Key Research Program of Frontier Sciences (QYZDB-SSW-SLH018), Recruitment Program of Global Experts, CAS Hundred Talent Program, Anhui Provincial Natural Science Foundation (1608085QB24), and China Postdoctoral Science Foundation (2015T80660). XAFS measurements were performed at the beamline BL14W1 in the Shanghai Synchrotron Radiation Facility (SSRF), China. DRIFTS and XPS measurements were performed at the Infrared Spectroscopy and Microspectroscopy Endstation (BL01B) and the Photoemission Endstation (BL10B) in the National Synchrotron Radiation Laboratory (NSRL) in Hefei, China, respectively.

REFERENCES

1. Aresta, M.; Dibenedetto, A.; Angelini, A. *Chem. Rev.* **2014**, *114*, 1709.
2. Maki-Arvela, P.; Simakova, I. L.; Salmi, T.; Murzin, D. Y. *Chem. Rev.* **2014**, *114*, 1909.
3. Kothandaraman, J.; Goeppert, A.; Czaun, M.; Olah, G. A.; Prakash, G. K. *J. Am. Chem. Soc.* **2016**, *138*, 778.
4. Posada-Perez, S.; Ramirez, P. J.; Evans, J.; Vines, F.; Liu, P.; Illas, F.; Rodriguez, J. A. *J. Am. Chem. Soc.* **2016**, *138*, 8269.
5. Ma, S.; Sadakiyo, M.; Heima, M.; Luo, R.; Haasch, R. T.; Gold, J. I.; Yamauchi, M.; Kenis, P. J. *J. Am. Chem. Soc.* **2017**, 139, 47.
6. Liu, R.; Stephani, C.; Han, J. J.; Tan, K. L.; Wang, D. W. *Angew. Chem. Int. Ed.* **2013**, *52*, 4225.
7. Roy, S. C.; Varghese, O. K.; Paulose, M.; Grimes, C. A. *ACS Nano* **2010**, *4*, 1259.
8. Habisreutinger, S. N.; Schmidt-Mende, L.; Stolarczyk, J. K. *Angew. Chem. Int. Ed.* **2013**, *52*, 7372.
9. Tu, W.; Zhou, Y.; Zou, Z. *Adv. Mater.* **2014**, *26*, 4607.
10. White, J. L.; Baruch, M. F.; Pander III, J. E.; Hu, Y.; Fortmeyer, I. C.; Park, J. E.; Zhang, T.; Liao, K.; Gu, J.; Yan, Y.; Shaw, T. W.; Abelev, E.; Bocarsly, A. B. *Chem. Rev.* **2015**, *115*, 12888.
11. Zhang, H.; Wei, J.; Dong, J.; Liu, G.; Shi, L.; An, P.; Zhao, G.; Kong, J.; Wang, X.; Meng, X.; Zhang, J.; Ye, J. *Angew. Chem. Int. Ed.* **2016**, *55*, 14310.
12. Meng, X. G.; Wang, T.; Liu, L. Q.; Ouyang, S. X.; Li, P.; Hu, H. L.; Kako, T.; Iwai, H.; Tanaka, A.; Ye, J. H. *Angew. Chem. Int. Ed.* **2014**, *53*, 11478.
13. Choi, K. M.; Kim, D.; Rungtaweevoranit, B.; Trickett, C. A.; Barmanbek, J. T.; Alshammari, A. S.; Yang, P.; Yaghi, O. M. *J. Am. Chem. Soc.* **2016**, *139*, 356.
14. Cao, Z.; Kim, D.; Hong, D.; Yu, Y.; Xu, J.; Lin, S.; Wen, X.; Nichols, E. M.; Jeong, K.; Reimer, J. A.; Yang, P.; Chang, C. J. *J. Am. Chem. Soc.* **2016**, *138*, 8120.
15. Kuhl, K. P.; Cave, E. R.; Abram, D. N.; Jaramillo, T. F. *Energ. Environ. Sci.* **2012**, *5*, 7050.
16. Jin, M.; He, G.; Zhang, H.; Zeng, J.; Xie, Z.; Xia, Y. *Angew. Chem. Int. Ed.* **2011**, *50*, 10560.
17. Friedrich, M.; Penner, S.; Heggen, M.; Armbruster, M. *Angew. Chem. Int. Ed.* **2013**, *52*, 4389.
18. Long, R.; Huang, H.; Li, Y.; Song, L.; Xiong, Y. *Adv. Mater.* **2015**, *27*, 7025.
19. Fan, Z.; Luo, Z.; Huang, X.; Li, B.; Chen, Y.; Wang, J.; Hu, Y.; Zhang, H. *J. Am. Chem. Soc.* **2016**, *138*, 1414.
20. Durst, J.; Simon, C.; Hasche, F.; Gasteiger, H. A. *J. Electrochem. Soc.* **2015**, *162*, F190.
21. Kyriakou, G.; Boucher, M. B.; Jewell, A. D.; Lewis, E. A.; Lawton, T. J.; Baber, A. E.; Tierney, H. L.; Flytzani-Stephanopoulos, M.; Sykes, E. C. *Science* **2012**, *335*, 1209.
22. Xu, Y.; Ruban, A. V.; Mavrikakis, M. *J. Am. Chem. Soc.* **2004**, *126*, 4717.
23. Bai, S.; Xie, M.; Kong, Q.; Jiang, W.; Qiao, R.; Li, Z.; Jiang, J.; Xiong, Y. *Part. Part. Syst. Charact.* **2016**, *33*, 506.
24. Nørskov, J. K.; Bligaard, T.; Rossmeisl, J.; Christensen, C. H. *Nat. Chem.* **2009**, *1*, 37.
25. Du, N.; Wang, C.; Wang, X.; Lin, Y.; Jiang, J.; Xiong, Y. *Adv. Mater.* **2016**, *28*, 2077.
26. Stamenkovic, V. R.; Mun, B. S.; Arenz, M.; Mayrhoffer, K. J. J.; Lucas, C. A.; Wang, G.; Ross, P. N.; Markovic, N. M. *Nat. Mater.* **2007**, *6*, 241.
27. Greeley, J.; Stephens, I. E. L.; Bondarenko, A. S.; Johansson, T. P.; Hanse, H. A.; Jaramillo, T. F.; Rossmeisl, J.; Chorkendorff, I.; Nørskov, J. K. *Nat. Chem.* **2009**, *1*, 552.
28. Ressler, T. *J. Synchrotron Radiat.* **1998**, *5*, 118.
29. Ankudinov, A. L.; Ravel, B.; Rehr, J. J.; Conradson, S. D. *Phys. Rev. B* **1998**, *58*, 7565.
30. Li, R.; Hu, J.; Deng, M.; Wang, H.; Wang, X.; Hu, Y.; Jiang, H. L.; Jiang, J.; Zhang, Q.; Xie, Y.; Xiong, Y. *Adv. Mater.* **2014**, *26*, 4783.
31. Kresse, G.; Furthmüller, J.; *Phys. Rev. B* **1996**, *54*, 11169.
32. Long, R.; Mao, K.; Gong, M.; Zhou, S.; Hu, J.; Zhi, M.; You, Y.; Bai, S.; Jiang, J.; Zhang, Q.; Wu, X.; Xiong, Y. *Angew. Chem. Int. Ed.* **2014**, *53*, 3205.
33. Yu, J.; Low, J.; Xiao, W.; Zhou, P.; Jaroniec, M. *J. Am. Chem. Soc.* **2014**, *136*, 8839.
34. Wu, W. Q.; Bhattacharyya, K.; Gray, K.; Weitz, E. *J. Phys. Chem. C* **2013**, *117*, 20643.
35. Garand, E.; Wende, T.; Goebbert, D. J.; Bergmann, R.; Meijer, G.; Neumark, D. M.; Asmis, K. R. *J. Am. Chem. Soc.* **2010**, *132*, 849.
36. Neatu, S.; Macia-Agullo, J. A.; Concepcion, P.; Garcia, H. *J. Am. Chem. Soc.* **2014**, *136*, 15969.
37. Su, W.; Zhang, J.; Feng, Z.; Chen, T.; Ying, P.; Li, C. *J. Phys. Chem. C* **2008**, *112*, 7710.

SYNOPSIS TOC